Stability of Cobalt Particles In and Outside HZSM-5 under CO Hydrogenation Conditions Studied by *ex situ* and *in situ* Electron Microscopy

Angela Straß-Eifert,[a] Thomas L. Sheppard,[b, c] Christian D. Damsgaard,[d] Jan-Dierk Grunwaldt,[b, c] and Robert Güttel*[a]

Designing stable materials for processes operating under harsh reaction conditions, like CO hydrogenation, is a challenging topic in catalysis. These may provoke several deactivation mechanisms simultaneously, like thermal sintering, oxidation or poisoning of the active sites. We report HZSM-5 supported cobalt catalysts, exhibiting cobalt nanoparticles encapsulated inside, or located at the exterior of the ZSM-5 support. The materials were studied by a combination of *ex situ* and *in situ* electron microscopy with respect to the growth of the cobalt particles. After 1200 h time on stream under CO hydrogenation conditions, the spent catalyst showed minimal sintering of encapsulated cobalt particles. *In situ* environmental TEM experiments under model reduction and CO hydrogenation conditions indicate the presence of cobalt nanoparticles, which appear highly resistant towards sintering even up to 700 °C. These results provide a first indication for the preparation of sinter stable catalysts suitable for operating in harsh reaction environments.

Introduction

Particle-shell catalysts are currently gaining significant attention in scientific research, offering a variety of advantages such as stabilizing metal nanoparticles against sintering, the possibility to tailor both physical and chemical functionalities, as well as to generate confinement effects.[1–3] The stabilization effect, in particular, makes such materials very attractive for use in industrially relevant reactions typically conducted under harsh conditions.[4–6] Further, the particle-shell materials offer the possibility to study the evolution of individual metal nanoparticles in technically relevant catalyst configurations, given by the well-defined spatial structure of those materials. Additionally, for these type of materials a confinement effect is reported, leading to improved stability and even selectivity.[7–10]

In the present contribution, the hydrogenation of CO towards hydrocarbons with cobalt based catalysts is chosen as a case study, which comprises the Fischer-Tropsch (FT) reaction as one important application in the field of heterogeneous catalysis. Typical reaction conditions cover a pressure range between 1 and more than 20 bar, as well as temperatures between 200 and 350 °C, depending on the desired hydrocarbon chain length. Low pressures and high temperatures favor methane formation, while low temperatures and high pressures are typical for FT synthesis for the formation of higher hydrocarbons.[4,10–13] The catalysts used under technical conditions consist of cobalt nanoparticles supported on porous substrates, such as silica or alumina.[14–17] More recently, zeolitic substrates are studied to a growing extent, as they offer acidic sites for cracking of long chain hydrocarbons formed under FT conditions.[18–20] Importantly, many catalysts suffer from deactivation under reaction conditions, due to various mechanisms including sintering at high temperatures and via carbonyl formation, as well as water induced re-oxidation or formation of carbon deposits.[21–25] The group of Bartholomew[26] recently summarized the state of knowledge on deactivation of cobalt catalysts for FT synthesis comprehensively and particularly pointed out that "*in situ* experimental methods for measuring NC size and size distribution with time on stream" are required for "further progress in the development of more sinter-resistant Co catalysts". Those methods are performed preferably as close as possible to typical operating conditions. However, the detailed molecular understanding remains a significant technical challenge.[27–30]

[a] *A. Straß-Eifert, Prof. R. Güttel*
Institute of Chemical Engineering
Ulm University
Albert-Einstein-Allee 11
89081 Ulm (Germany)
E-mail: robert.guettel@uni-ulm.de
[b] *Dr. T. L. Sheppard, Prof. J.-D. Grunwaldt*
Institute for Chemical Technology and Polymer Chemistry
Karlsruhe Institute of Technology
Engesserstr. 20
76131 Karlsruhe (Germany)
[c] *Dr. T. L. Sheppard, Prof. J.-D. Grunwaldt*
Institute of Catalysis Research and Technology
Karlsruhe Institute of Technology
Hermann-von-Helmholtz Platz 1
76344 Eggenstein-Leopoldshafen (Germany)
[d] *Prof. C. D. Damsgaard*
DTU Nanolab and DTU Physics
Technical University of Denmark
Fysikvej – Building 307
2800 Kongens Lyngby (Denmark)

Supporting information for this article is available on the WWW under https://doi.org/10.1002/cctc.202001533

One of the most attractive techniques for characterization on an atomic scale is transmission electron microscopy (TEM), as it provides spatially-resolved information on the cobalt nanoparticle size distribution and the morphology.[31] In particular, environmental TEM (ETEM) allows investigation of the catalyst evolution under controlled gas environment and elevated temperatures. Through differential pumping to commercial microscopes operating up to 300 kV, atomically-resolved images of supported metal catalysts operating with gas pressures up to approx. 10 mbar and temperatures up to 1000 °C can be acquired *in situ*.[32] Alternatively, by using closed gas cell nanoreactors it is possible to perform *operando* TEM measurements at 0.1–5 bar. Compared to ETEM this method involves even more challenging sample preparation as the sample has to be positioned inside the nanoreactor.[33–35] In both cases catalyst behavior in a model operating environment can be examined. In literature, there are already several ETEM[36] studies with emphasis on CO hydrogenation reactions available for Co-based catalysts.[37–41] For example, Mitchell et al.[37] investigated the effect of pretreatment methods on the nanostructure and catalytic performance of supported cobalt catalysts prepared by impregnation. The authors found a correlation between hexagonal (hcp) cobalt sites and the activity of the catalyst. In another study, Li et al.[38] reported the *in situ* synthesis of non-promoted and Ru promoted Co/Al_2O_3 catalysts. Besides the reported changes in morphology and particle size during the reduction phase of the catalyst, the initial contact between the catalyst and the reactant mixture (typically H_2:CO = 2:1) during CO hydrogenation was even more important for catalyst evolution and the achievable activity. Schulz et al. postulated an *in situ* construction of the "true" cobalt catalyst surface in this initial stage with changes in reaction rate and selectivity induced by surface segregation through strong CO chemisorption.[42] But studies on the behavior of cobalt particles in syngas environment are scarce. Recently, Dembélé et al. published an *in situ* TEM study investigating the thermal behavior and surface reactivity of cobalt nanoparticles supported on silicon doped Al_2O_3 in syngas environment.[41] They detected a build-up of carbon layers on the cobalt surface at higher temperatures (400–450 °C) due to CO disproportionation. Although ETEM studies are typically limited to a low pressure range and there is a gap in the experiment duration, it can provide an important complementary insight into deactivation to *operando* studies as it allows to monitor changes at the atomic scale.[33] Additionally, the capability of *in situ* TEM to track the time dependent evolution of individual particles under model conditions is complementary to *ex situ* TEM providing cumulative information after exposure to technicaly-relevant conditions.

In this contribution we present a detailed *in situ* and *ex situ* TEM investigation on a cobalt-based catalyst material with tunable particle size, synthesized via a previously reported bottom-up approach.[18] The bifunctional Co/HZSM-5 catalyst was designed to produce cobalt particles in different locations within the zeolite matrix, in order to investigate the stability behavior as a function of the locus. CO hydrogenation was chosen as model reaction, since it suffers from various deactivation mechanisms, such as thermal sintering. First, the catalytic activity of the material was investigated under CO hydrogenation conditions typical for FT reaction (200–250 °C, 20 bar, H_2:CO = 2) over a period of ca. 1200 h. The spent catalyst was investigated via *ex situ* TEM to examine average changes in cobalt particle size, probing the catalyst transformation after reaction. Second, complementary ETEM experiments under model conditions (1.2 mbar) were performed to directly monitor changes of individual cobalt nanoparticles as a function of time-on-stream and location within the zeolite matrix. The aim was to probe sinter stability and resistance to degradation depending on the local environment of the cobalt particles.

Experimental Section

Synthesis of Co/HZSM-5

The catalyst material was synthesized via a bottom-up synthesis route, described by Kruse et al.[18] Material A (Co_3O_4 nanoparticles, Figure S6) was prepared via a solvothermal treatment of a mixture of 3.32 g Co-nitrate (Cobalt(II) nitrate hexahydrate, > 97.7 %, Alfa Aesar) and 6.64 g polyvinylpyrrolidone (PVP, MW 1.300.000, high purity grade, Amresco) dissolved in 375 mL ethanol (96 vol-%, VWR Chemicals) at 180 °C in a teflon-lined autoclave for 3 h. Subsequently, 50.0 g of the resulting cobalt oxide suspension was dissolved in an ethanol/water mixture (60/40 vol.) together with 1.95 g cetyltrimethylammoniumbromide (CTAB, high purity grade, Amresco) as porogen. Basic media conditions were adjusted by addition of 12.4 mL aqueous ammonia solution (NH_{3aq}, 30 % p.a. ACS, Carl Roth). Afterwards, 6.40 mL of the silicon source tetraethylorthosilicate (TEOS, for synthesis, Merck) were added dropwise under stirring. After stirring for 2 h at room temperature the formed solids were collected via centrifugation and washed three times with distilled water, followed by calcination at 500 °C (heating ramp 2 °C min^{-1}) for 6 h leading to Co_3O_4@$mSiO_2$ particle-shell particles (material B; Figure S7). In the last synthesis step material B was used as precursor for the hydrothermal zeolite synthesis, leading to the final Co_3O_4/HZSM-5 catalyst (material C). Therefore, the solids were dissolved in an aqueous mixture of sodium hydroxide (25 wt% solution, ≥ 99 % p.a., Carl Roth), the aluminum source sodium aluminate (water free, technical grade, Alfa Aesar), as well as tetrapropylammoniumhydroxide (TPAOH, 40 % w/w aq., Alfa Aesar) as structure directing agent and sulfuric acid (0.1 M, for analysis, Merck) for adjusting the pH. The reaction mixture with a molar ratio of 1.0000 SiO_2:0.0056 Al_2O_3:0.0193 Na_2O:0.4285 TPAOH:0.0204 H_2SO_4:42.6244 H_2O:0.4171 OH^- was treated at 175 °C for 30 h in a teflon-lined autoclave. Afterwards the product was collected by centrifugation, purified and calcined at 500 °C (heating ramp 2 °C min^{-1}) for 6 h. The H-form of the zeolite was obtained by ammonia ion exchange, treating the material three times in 1 M NH_4NO_3 solution (≥ 98 % p.a. ACS, Carl Roth) at 60 °C for 60 min, and a second calcination step at 500 °C as described before.

Catalyst Characterization

For scanning electron microscopy (SEM) measurements a *Hitachi S-5200* electron microscope was used. The samples were prepared by dropping 20 μL of catalyst suspension in ethanol on a silicon wafer glued to a SEM sample holder; the electrical contact between sample holder and wafer was achieved by use of conductive silver paste. Focused ion beam (FIB) preparation of a lamella was

performed in a dual beam FIB/SEM chamber (*Helios Nanolab 600; Thermo Fisher Scientific*) by cutting a 100 nm slice of some zeolite crystals and glueing it to the edge of a TEM grid from *Omniprobe*. TEM images were taken on a Jeol 1400 microscope operating at 120 kV. X-ray powder diffraction (XRD) patterns were recorded on a *Philips* diffractometer and on a *STOE STADI-p* diffractometer equipped with a *DECTRIS MYTHEN 1 K* strip detector using Cu–Kα radiation (λ = 1.54184 Å) with 40 kV and 30 mA, respectively. The measurements were performed in the 2θ interval 2–90° and 0–70° in steps of 0.015°. Nitrogen adsorption and desorption measurements were executed at liquid nitrogen temperature (77 K) using a high-resolution *Micromeritics 3Flex* instrument with a special micropore port equipped with a 0.1 Torr pressure transducer. Prior to the measurement the samples were degassed under vacuum at 300 °C for 4 h. Brunauer-Emmett-Teller (BET) Rouquerol method was applied for determination of the surface area. For mesopore evaluation the method after Barret-Joyne-Halenda (BJH) was used. The micropore size distribution was determined by the Horwath-Kawazoe model. Elemental analysis was done via inductively coupled plasma optical emission spectrometry (ICP-OES) and graphite furnace atomic absorption spectroscopy (GFAAS) measurements. Therefore, the powder sample was dissolved in a mixture of 8 mL HF, 2 mL HNO_3 and 2 mL HCl. The resulting solution was measured in a *Spectro Spectroflame Modula 200* including a Cross-flow-Vaporizer and an Echelle-Monochromator for ICP-OES and in an atomic absorption spectrometer *PE 1100 B* from *Perkin Elmer* using an aluminum hollow cathode lamp for GFFAAS. The X-ray photoelectron spectroscopy (XPS) measurements were conducted at a PHI 5800 ESCA device. Monochromatized Al–Kα radiation (1486.6 eV) at an emission angle of 45° was used gaining analyzer pass energy of 93.9 eV for the survey spectra.

CO hydrogenation activity tests were performed using a slit-shaped microreactor (slit width 1 mm) operated under isothermal conditions and in a packed bed reactor, as previously described in detail.[43] Prior to the catalytic experiment 500 mg of the catalyst were pelletized, crushed and sieved to a fraction of 90 to 180 μm. The catalyst was reduced at 350 °C under pure hydrogen at ambient pressure for 16 h. After cooling to 150 °C the continuous activation and reaction phase was started by increasing the pressure to 2.1 MPa with a CO flow rate of 0.5 $L_{STP}h^{-1}$ and a H_2/CO ratio of 2. Online gas analysis was performed by a Varian CP-3800 gas chromatograph (GC) equipped with a thermal conductivity and flame ionization detector to analyze the permanent gases and gaseous hydrocarbons, using Ar as internal standard as described previously.[43]

Ex situ TEM

Ex situ TEM measurements were performed on a *Jeol 1400* microscope operating at 120 kV. The TEM samples were prepared by suspending a small amount of catalyst powder in ethanol under ultrasonication. One droplet of the resulting suspension was applied to a graphitized copper grid (200 mesh). Additionally, TEM images of 80 nm thick lamellas of the zeolite particles were taken after embedding a small portion of the catalyst powder in epoxy resin, mechanical cutting a slice by microtomy and placing the resulting lamella on a copper grid. Typically, around 200 particles were considered for the statistic evaluation of the cobalt oxide/cobalt particle size distribution using the software *ImageJ* for image processing.[44]

In situ TEM

Prior to the measurement in the ETEM the zeolite crystals in the as-prepared material C were cut into thin cross-sections by Focused Ion Beam milling and micromanipulation at the FIB Center of Ulm University (Ulm, Germany). The procedure is summarized in SI (Figure S1-5, SI). First, material C powder was fixed to a standard SEM stub sample holder using a conductive silver resin (*ACHESON 1415, Plano*) and introduced to the dual beam FIB-SEM chamber (*Helios Nanolab 600, Thermo Fisher Scientific*). Second, suitable particles were preselected and bound together via ion beam assisted deposition of Pt. Afterwards, the selected particles were thinned into a cross-section of ~100 nm thickness using a Ga^+ ion beam at 30 kV. The resulting cross-section containing several slices of material C was placed across the Si_3N_4 membrane window of a Wildfire heating chip (*DENS solutions*) and fixed to the wall of the window by ion beam assisted deposition of Pt. The procedure was repeated several times to prepare several individual, sample-loaded chips. Note that the FIB procedure could possibly contaminate the sample with Pt, Ga or Ag. It should also be noted that unlike previous TEM examples of supported cobalt catalysts, where the catalyst powder was typically crushed to ensure suitable transmission path length of the electron beam for TEM, the bifunctional catalysts here were necessarily used intact. Although this greatly limits the resolution obtained due to electron attenuation by the relatively large catalyst grains, it was considered necessary to preserve the bifunctional catalyst structure to accurately determine the behaviour of the cobalt particles in different locations within the zeolite matrix.

The ETEM experiments were performed at DTU Nanolab at the Technical University of Denmark (DTU, Kgs. Lyngby, Denmark) using a Titan E-Cell 80–300 ST TEM (*FEI*) operating at 300 keV. The electron dose rates were between approximately 300 and 500k $e^- nm^{-2} s^{-1}$ depending on the magnification. The image acquisition time was 1 s. To rule out beam induced degradation prior to the experiment a beam stability test was conducted on a different sample spot and the electron dose rate and acquisition time were adjusted. The samples prepared on chips were loaded into the Wildfire sample holder (*DENS solutions*) and inserted into the ETEM. Temperature was controlled using the integrated heating system of the Wildfire holder. Gases were supplied by mass flow controllers in a differential pumping scheme. The gas composition flowing through the cell was monitored using a mass spectrometer capillary positioned close to the sample to confirm the correct gas environment. Standard and high resolution (HRTEM) TEM images were acquired under the following conditions: (i) under vacuum at 20 °C; (ii) under 1.2 mbar H_2 flow from 20 to 400 °C; (iii) under 1.2 mbar H_2:CO (2:1) flow from 150 to 1000 °C. Between changes in gas environment, the system was left to equilibrate for 40–60 min until the detected signal by mass spectrometry was constant. The specific conditions at which images were acquired are indicated in the relevant figure captions. Images were processed using Digital Micrograph software (Gatan) and ImageJ.[44] Particle size distributions were determined by manual counting of individual cobalt features and approximating these as circular.

Results and Discussion

Catalyst Characterization

A representative SEM image of material C is presented in Figure 1a, which reveals well-defined zeolite crystals of about 1–2 μm in size showing some cobalt oxide particles on the external zeolite surface. In Figure 1b and c the TEM images of a slice of material C cut via FIB is shown, revealing homogeneously dispersed cobalt oxide particles inside the zeolite

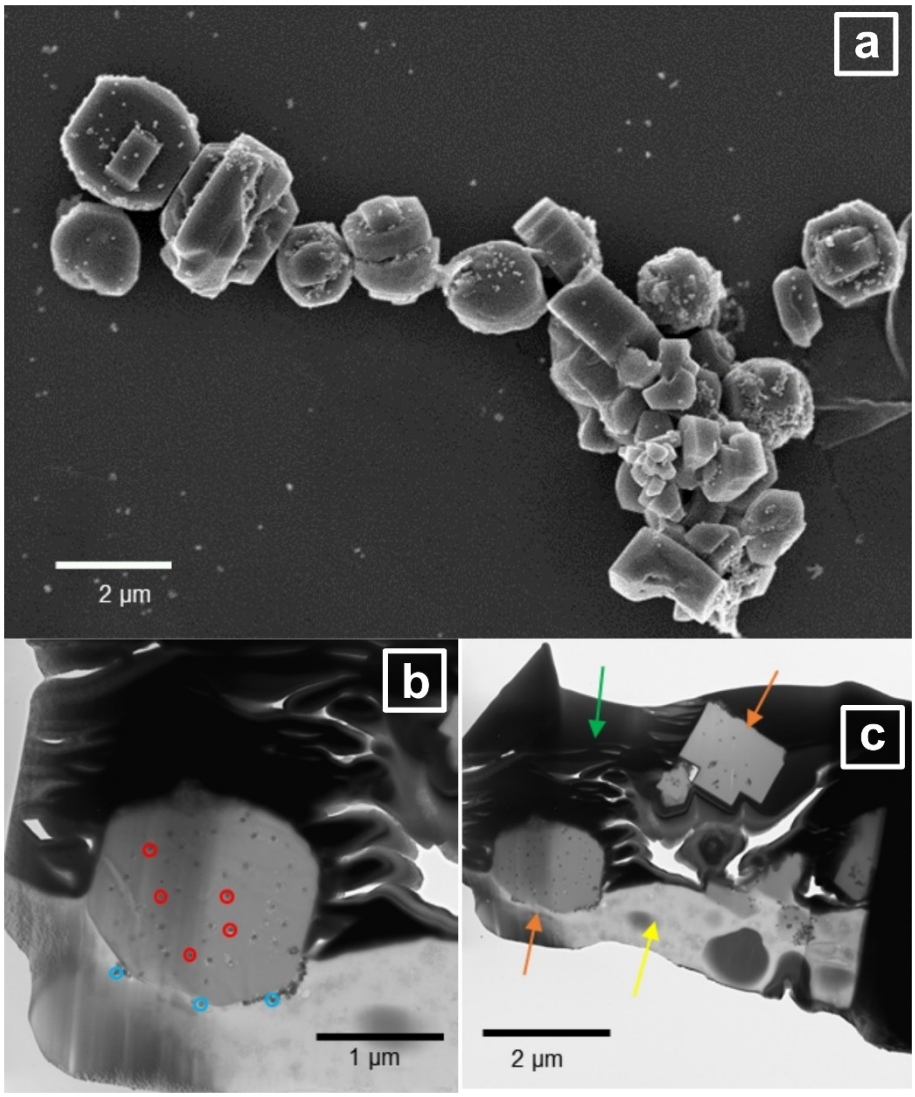

Figure 1. (a) SEM image of material C and (b, c) TEM images of zeolite slices in Ag resin (yellow arrow) embedded crystals of material C (orange arrows) bonded via ion beam assisted Pt deposition (green arrow) and cut via FIB.

matrix (red circles) and some cobalt oxide particles at the external zeolite surface (blue circles).

The TEM images and particle size distributions of material A and B are presented in the supporting information (Figure S6 and S7). While the cobalt oxide particle size determined from material B shows a mean particle size of about 46 ± 10 nm, the particle size determined from material C appears to be slightly smaller (40 ± 7 nm). The observed difference could be a result of the basic synthesis conditions and possible dissolution of cobalt oxide particles. Evaluation and discussion of the results is based on the particle size derived from material C. Notably, the cobalt oxide particles still indicate the presence of agglomerated nanoparticles about 12 nm in size at all stages of the synthesis procedure (Figure S6). The powder XRD of material B (Figure S8, SI) shows the characteristic reflections for Co_3O_4 and the hexagonal mesopore structure of amorphous SiO_2. In contrast, the diffractogram of material C (Figure S9, SI) displays the characteristic reflections of HZSM-5, along with those of Co_3O_4 crystallites. This demonstrates the successful conversion of amorphous silica into crystalline zeolite. Estimation of the cobalt oxide crystallite size by the Scherrer equation using full width at half maximum (FWHM) for the (311) reflection at 36.6° 2θ results in a crystallite size of approximately 30–31 nm. This value is between the sizes of the primary cobalt oxide particles of ca. 12 nm and that of the agglomerates of about 40 nm as determined by TEM, which is consistent considering the rather broad and potentially bimodal size distribution of the cobalt oxide particles and the averaging nature of powder XRD analysis. Physisorption experiments of material B (Figure S10, SI) show a mesoporous material with a BET surface area of 988 ± 60 m^2/g and an average pore size of 2.5 nm determined via BJH from the desorption branch. The nitrogen sorption isotherm of material C (Figure S11, SI) exhibits a Type I behavior, characteristic for micropore adsorption at low relative pressures between

10^{-6} and 0.1 p/p_0, resulting in a micropore size of 9.3 Å and a BET surface area of 395 m^2/g calculated by use of the Rouquerol plot. Both values for pore size and surface area are significantly smaller than for material B and typical for zeolitic materials, also confirming the morphology change. The results of the quantitative analysis via ICP and GFAAS indicate a cobalt metal content of 9.9 wt%, which is slightly higher than the theoretically calculated value of 8.4 wt%. The Si/Co ratio of 7.2 is smaller than the nominal value of 10.6, due to silicon losses during the preparation method. The measured Si/Al ratio of 1250 is significantly different from the theoretical value of 890, which could be caused by either partial Al incorporation during zeolite crystallization or errors in the GFAAS measurement, due to losses of Al during acidulation. The atomic concentration of surface elements was also determined via XPS (Table S1). The achieved surface ratios can be compared with those determined via bulk analysis. The Si/Al ratio of 440 at the surface compared to a ratio of 1250 determined in the bulk indicates that the zeolite crystals exhibit a silicon rich core and an Al rich shell, most probably caused by the transformation process during conversion of material B into C. The Si/Co ratio of 4 is smaller than the ratio determined for the bulk, which points towards a silicon poor zeolite shell. The reducibility of material C was investigated by means of H_2 temperature programmed reduction (TPR) showing peaks in the range between 200 and 400 °C (Figure S12) and proving successful reduction of cobalt oxide to metallic cobalt.

The catalytic activity of material C for CO hydrogenation was determined at reaction temperatures up to 250 °C and for 1200 h time on stream (TOS), see Table 1. As expected, the CO conversion and methane selectivity increase with temperature reaching maximum values at 250 °C. While the CO conversion appears to be stable even at 250 °C, the selectivity of methane decreases and that of carbon dioxide increases, between 800 and 1200 h TOS. This observation will be discussed below in context with the findings from ETEM studies under model reaction conditions. Furthermore, compared to our previous results[18] the methane selectivity observed here is relatively high. One reason could be hydrogenolysis of paraffins, which causes the successive demethylation at the end of the hydrocarbon chain forming CH_4 and a heavier fragment, as reported for Co-based catalysts with a zeolitic support.[45–47] Another reason could be the counter diffusion of reactants and products in the microporous structure, which might lead to a high H_2/CO ratio at the active cobalt nanoparticle sites, eventually causing higher methane selectivity.[48,49] Furthermore, the cobalt time yield (CTY) was calculated, which is in good agreement with values from Kang and co-workers[50] investigating impregnated Co/HZSM5 at comparable conditions (in particular at 240 °C). In addition, the CTY is comparable to our earlier work,[18] where diffusion limitations could be excluded by determination of the apparent activation energy being in a reasonable range for cobalt catalysts.

Ex situ TEM

For cumulative evaluation of morphology changes and evolution of the cobalt particle size distribution after exposure to real reaction conditions, the fresh and spent catalysts were analyzed *ex situ* by TEM and compared (Figure 2). It has to be considered that the fresh samples probably contain mainly cobalt oxide, while for the spent ones in addition to metallic cobalt also cobalt oxide may be present, due to the exposure to air during transfer from the reactor to the microscope.[25] The comparison reveals no changes in the zeolite crystal, while a more pronounced appearance of cobalt particles at the external particle surface and larger aggregates were observed for the spent sample. The latter could be explained by sintering of cobalt particles located at the external surface of the zeolite crystal. In contrast, cobalt particles encapsulated within the zeolite matrix still appear well-dispersed after reaction (Figure 2c, 2d). The different evolution of cobalt particles dependent on being embedded in the zeolite matrix or not can also be concluded by the cobalt particle size distribution evaluated from the different locations within the zeolite matrix. While the distribution is rather comparable for cobalt oxide particles irrespective of location for the fresh material (40 ± 7.0 nm for encapsulated species, 40 ± 7.5 nm for external surface particles) (Figure 2e), a significant growth of the non-encapsulated cobalt particle fraction can be observed after reaction along with a broader distribution (46 ± 16 nm), compared to shrinkage of the embedded particles (27 ± 7.0 nm) (Figure 2f). Note that the oxidic layer formation was not considered, although we expect a thin cobalt oxide layer on the spent catalyst.

The observed decrease of the mean particle size for the encapsulated particles (ca. 30 %) is due to the reduction of Co_3O_4 to metallic cobalt (density based size ratio $Co^0 : Co_3O_4 = 0.75$).[51] The strong increase and broadening of the size distribution observed for the external particles, however, clearly points towards severe particle growth by sintering or Ostwald ripening under reaction conditions. It has to be mentioned that

Table 1. CO conversion (X_{CO}), CH_4, C_{2+} and CO_2 selectivities (S_{CH4}, $S_{C_{2+}}$, S_{CO_2}) and cobalt time yield (*CTY*) of material C during CO hydrogenation, operating conditions: 20 bar, H_2:CO 2:1, 0.5 L_{STP}/h CO, 500 mg catalyst.

TOS (h)	*T* [°C]	X_{CO} [%]	S_{CH_4} [%]	S_{CO_2} [%]	$S_{C_{2+}}$ [%]	$CTY/10^{-5}$ [$mol_{CO}\,g_{Co}^{-1}\,s^{-1}$]
390	200	4.0	37.0	3.0	60.0	0.45
439	210	4.7	43.0	5.9	51.1	0.53
553	220	8.6	52.3	7.2	40.5	0.96
586	230	9.5	51.1	7.0	51.9	1.07
733	240	16.9	53.7	5.7	40.6	1.90
799	250	19.9	64.6	4.6	30.8	2.23
1206	250	19.5	57.4	8.5	34.1	2.19

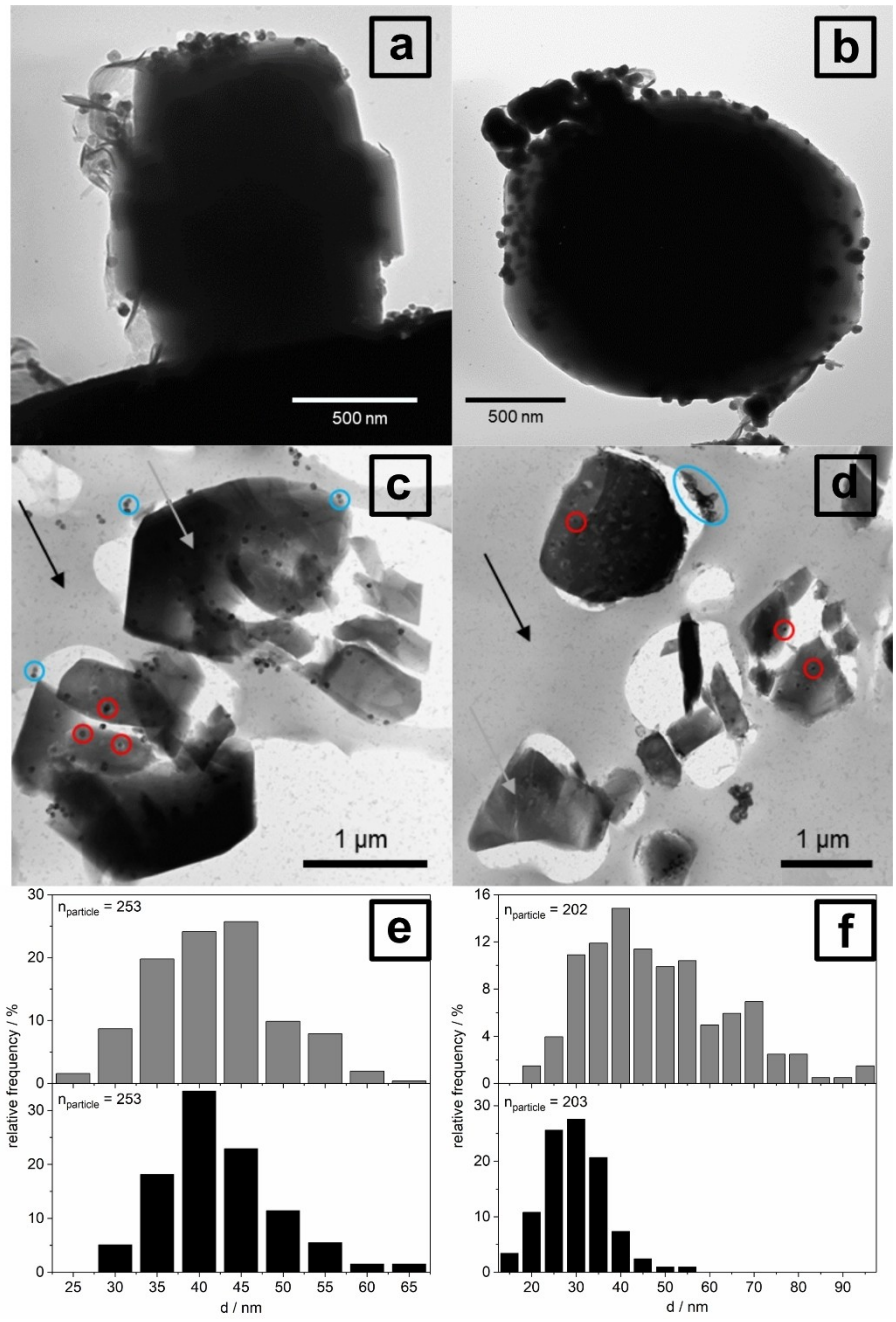

Figure 2. TEM images of zeolite crystals (a, b) with cobalt oxide and cobalt particles, and mechanically cut 80 nm slices of the crystals (c, d) embedded in epoxy resin, as well as cobalt oxide and cobalt particle size distribution of material C before (a, c, e) and after (b, d, f) CO hydrogenation; cobalt oxide or cobalt particles at the external surface (blue circles, grey plot in e and f) are distinguished from those encapsulated in the zeolite crystal (red circles, black bottom plot in e and f); grey arrow: zeolite crystal, black arrow: epoxy resin.

the differences in sintering behavior are clearly observed for cobalt particles in the size range of 40 nm, even though these are less prone to sintering compared to smaller ones according to Wolf et al.[52] The differences in sintering behavior can thus be attributed to the stabilizing effect of the zeolite matrix, as previously reported by Liu and Zhang.[53,54] This stabilizing effect is probably even more pronounced for smaller cobalt nanoparticles in the optimal size range for CO hydrogenation (5 to 10 nm),[55] although only larger particles were investigated in the current work. Note that the encapsulated species are accessible to the reactants and active during CO hydrogenation, confirmed by TPR measurements (Figure S11) and the observed void formation after reduction (Figure S14). Furthermore, Carvalho et al. reported comparable observations under similar reaction conditions, showing accessibility of the cobalt particles for the reaction intermediates.[56] Additionally, no phase change of the cobalt particles during reaction conditions is expected as also reported by Nie et al.[57]

In situ TEM

Reduction in H_2 atmosphere

In a first set of ETEM experiments the catalyst was studied during the reduction phase under H_2 atmosphere. Prior to those environmental conditions images were initially acquired under vacuum (10^{-8} mbar) at 20 °C. The particles in the as-prepared sample were expected to consist mostly of cobalt oxide (Co_3O_4 is suggested from XRD analysis in Fig. S9), therefore this condition was intended to serve as a baseline measurement before subsequent reduction and activation. The average particle size of the cobalt oxide particles was estimated by counting particles visible within a certain threshold distance from where the lamella was glued to the window of the chip (for an overview on the lamella see Figure S13, SI), in order to minimize miscounting possible contaminants as cobalt clusters. The average particle size based on counting 83 individual particles from 3 separate zeolite crystals was around 45 ± 5 nm (see Figure S15, SI). This result is in general agreement with *ex situ* TEM evaluation for cobalt oxide particles of the fresh catalyst

After the initial image recording, H_2 was introduced to the sample at 1.2 mbar via differential pumping across the chip surface. Images were acquired initially at 20 °C until stabilization of the H_2 signal was detected by mass spectrometry, which lasted around 40 min. The sample was then gradually heated from 20 to 400 °C over 10 min (~40 K/min), followed by reduction at 400 °C for a total of 2 h. Notably, upon reaching 400 °C a distinct difference was observed between the cobalt particles. Namely, some of the cobalt particles appeared to disintegrate forming several agglomerated smaller particles. This effect was confined to a localized area but with a clear composition of much smaller cobalt clusters (Figure 3). This behavior resembles the aggregated cobalt particles observed during TEM analysis of the precursor material A and material B (see Figure S6, S7, SI). In contrast to this, numerous other particles apparently remained intact. Note that the lattice structure appearing in Figure 3 b and c corresponds to zeolite lattice spacing visible depending on zone axis.

The different behavior could be in part influenced by contamination of the lamella with Pt, Ga and Ag due to the FIB preparation and the fixation of the sample onto the holder. But since the disintegration effect appeared rather randomly throughout the lamella, and was not confined to specific regions, we are confident that changes induced are a result of differences in the chemical environment of different particles and not caused by the presence of contaminants (visibly more concentrated towards the exterior of the lamella) or by beam effects. Another possible reason could be the relative position of the cobalt particles within the zeolite lamella. Based on *ex situ* TEM analysis, it was expected that particles located deep within the lamella far from the surface are unable to increase significantly in size or shape, due to the steric constraints of the microporous zeolite lattice. On the other hand, due to the FIB milling, statistically several of the particles observed would be expected to be close to or breach the surface of the lamella. As the same exact environmental conditions were applied to the entire lamella, the different behavior of these particles may indicate a different structural environment. Additionally, the breakup and rearrangement of cobalt particles when exposed to syngas may result in spreading and the formation of smaller particles in the vicinity of the original particles.[58]

Model Reaction Conditions

Following reduction and restructuring of a portion of the cobalt particles, the sample was cooled to 150 °C and model reaction conditions were applied (2:1 H_2:CO, 1.2 mbar). The sample was heated in two phases: firstly from 150 to 500 °C at ~7 K/min, then stepwise from 500 to 1000 °C with images acquired at 100 °C intervals (Figure S16, SI). In order to monitor the behavior of the cobalt species, particle size distribution was calculated throughout the experimental conditions applied. It should be noted that in order to avoid inconsistent results, only particles which did not show evidence of disintegration were included in

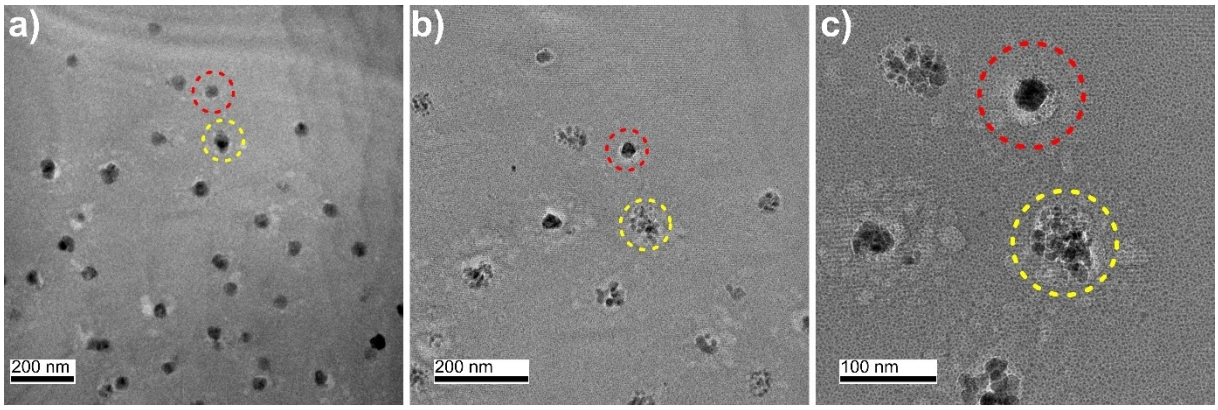

Figure 3. Material C investigated by ETEM showing disintegration (yellow circle) of some cobalt species and no significant disintegration (red circle) of others between (a) 20 °C and (b, c) 400 °C in 1.2 mbar H_2 with higher magnification in c); total electron dose ~2000 e^-/nm^2.

the counting, therefore the total number of individual particles counted was lowered from 83 (in vacuum conditions at the start of the study) to 20. The intact cobalt particles were therefore regarded as stable and were of greater interest for the purposes of monitoring possible sintering behavior at high temperature. To ensure accuracy in any changes observed, the initial particle size of this limited counting set was recalculated based on the images acquired initially under vacuum. As a result, the particle size changed following reduction in 1.2 mbar H_2 at 400 °C from around 44.8 ± 1.3 nm to 38.8 ± 1.3 nm, a decrease of around 15% (Figure 6). This is not fully consistent with the theoretical particle size reduction of pure Co_3O_4 to pure metallic cobalt (25%) and could indicate that the particles were not completely reduced by H_2 treatment. It is already reported in literature that the extent of reduction depends on the particle size, with smaller particles said to be more difficult to fully reduce.[59,60] The size reduction, however, proves the particles to be accessible by reactive gas and thus to take part in reaction. Furthermore, the comparison of the cobalt particle sizes measured *ex situ* (27.0 ± 7.0 nm) after reaction and *in situ* (38.8 ± 1.3 nm) after reduction conditions reveals a slight difference when taking the error bars, representing the standard deviation of the particle size distribution, into account. On the one hand the observed difference could result from the different reduction conditions being atmospheric pressure in pure H_2 for 16 h for the *ex situ* sample and at 1.2 mbar in H_2 for 2 h for the *in situ* sample, probably resulting in different degrees of reduction. On the other hand, there is a large difference in the number of particles counted (220–250 particles for the *ex situ* sample and 20 intact particles for the *in situ* sample) contributing to the particle size distribution and the resulting standard deviation. Additionally, the particles experienced different conditions as the *ex situ* sample underwent 1200 h realistic reaction conditions before being studied by TEM.

As shown in Figure 4, changing from 400 °C and pure hydrogen atmosphere (2) to 150 °C and syngas (3) resulted in a slight decrease in particle size from 38.8 ± 1.3 nm to 36.3 ± 1.3 nm. This is likely to be significant within error. After introduction of the reaction mixture at 150 °C and heating up to 500 °C (TEM image at 500 °C, Fig. S17, SI), a gradual increase in particle size (41.5 ± 1.3 nm) was observed (5), staying almost constant at higher temperatures (6,7). This could indicate the partial reoxidation of cobalt species resulting from CO disproportionation, proposed to occur as one step in the mechanism for hydrocarbon formation during CO hydrogenation.[25] This result is supported by HRTEM observations at 700 °C detecting ordered layers likely to be carbon (Figure S18, SI). Furthermore, Claeys et al.[25] investigated the sintering of catalyst nanoparticles at typical FT conditions and proposed a CO-assisted sintering via a surface subcarbonyl-type mechanism, pointing towards cobalt particle sintering in presence of CO. In addition, during an ETEM study on promoted cobalt oxide supported on alumina, Dehghan et al.[40] observed a high reactivity of cobalt nanoparticles and the tendency to reoxidize in traces of water even at room temperature. Since water is the main by-product of CO hydrogenation, traces could be built under ETEM conditions making reoxidation a possible deactivation mechanism.

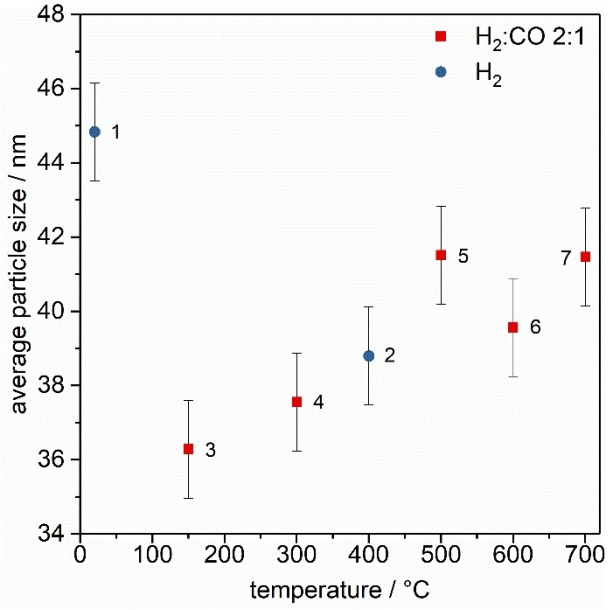

Figure 4. Particle size distribution of stable cobalt particles as a function of gas environment and temperature applied; results are based on individual counting of 20 intact cobalt particles, as first observed following reduction in H_2 at 400 °C; numbers indicating the chronology.

Following application of reaction temperatures up to 250 °C as for the *ex situ* study, the cobalt particle behavior and stability was observed under relatively harsh treatment conditions at 700 °C. These conditions are chosen to accelerate possible aging and sintering effects for the ETEM studies and could occur on technical scale during thermal run-away of cobalt catalyzed CO methanation. Several regions of interest were marked directly on reaching 700 °C (Figure 5a, c, e) and monitored again after approximately 66 min (Figure 5b, d, f). Additional high resolution images of Figure 5a and c upon reaching 700 °C are presented in the SI (Figure S18). The results show a diverse range of cobalt particle behaviors, as highlighted in Figure 5. Firstly, considering those particles labelled as intact following initial reduction, no apparent differences in size or shape were observed after 1 hour at 700 °C (red circles). This indicates that such intact particles were in fact highly stable towards sintering or degradation even at the relatively harsh conditions applied, possibly due to their location deep within the zeolite structure and the local absence of possible FIB contaminants. At the same time, several particles which disintegrated following initial reduction also remained in a highly dispersed state and did not react to the temperature conditions applied (yellow circles). However, other dissociated particles were seen to recombine into denser agglomerates (green circles), while clear evidence of Ostwald ripening was visible on neighboring particle clusters (pink circles). Kristamurthy et al. reported Ostwald ripening on planar Co/SiO_2 catalysts under FT conditions as a rapid sintering mechanism for small cobalt nanoparticles,[61] while larger nanoparticles are reported to sinter more slowly by crystallite

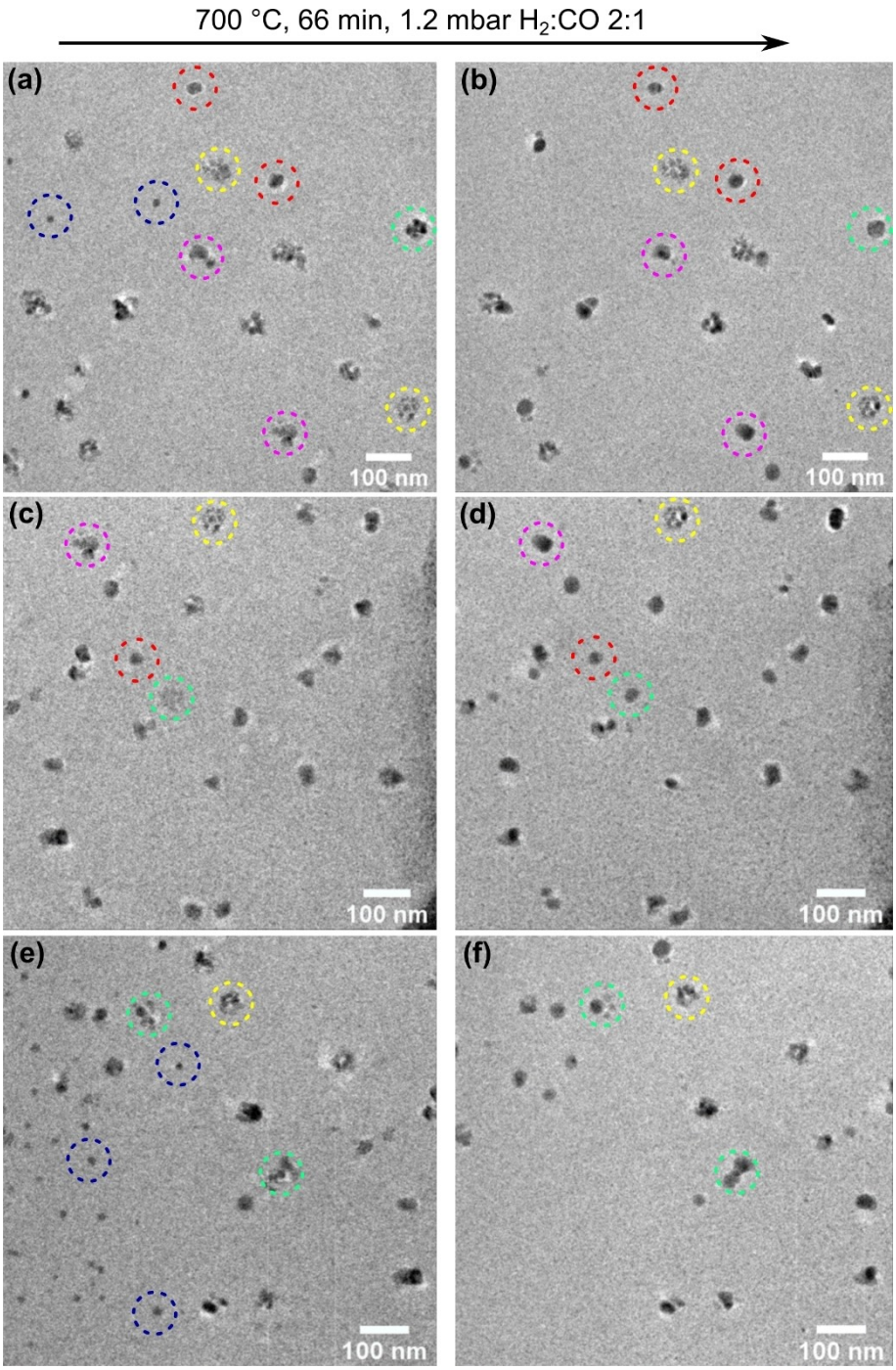

Figure 5. TEM images under a 1.2 mbar flow of H_2:CO 2:1 ratio; images (a), (c) and (e) show three regions of interest directly on reaching 700 °C; (b), (d) and (f) are the respective regions of interest after 66 min treatment at 700 °C; colored circles around individual cobalt particles indicate their classification as 'stable' (red), 'ripening' (pink), 'recombining' (green), 'disintegrated' (yellow) or 'disappearing' (blue); total electron dose ~2000 e^-/nm^2.

migration and coalescence.[26] The broad range of behaviors, mainly affecting the disintegrated particles, further indicates different physical environments present for the visible particles within the regions of interest. Furthermore, there were additional particles noticeable (blue circles in Figure 5a, e), showing clearly smaller diameters than the cobalt particles, appearing to decompose after 66 min at 700 °C. These small particles might be due to the contamination of the lamella during the preparation procedure either from the Ag resin or the Pt ion beam deposition from FIB, detected via TEM–EDX (Figure S20, SI). At higher temperatures these particles decompose and therefore disappeared. The contamination of the lamella due to the preparation method, also observed by HRTEM (Figure S19, SI), remains a challenge and the influence of the contaminants

like Ag, Pt and Ga on the behavior of the cobalt nanoparticles and especially on the reduction as discussed earlier cannot be ruled out. However, this is expected to be less significant for those particles contained within the zeolite structure, i.e. intact particles not exposed to the surface of the lamella.

To further investigate the differences between the cobalt particle behaviors observed, additional HRTEM images were obtained approximately 40 to 50 min after reaching 700 °C. Intact particles, disintegrated particles, and particles in an apparent intermediate state were defined as regions of interest (Figure S19, SI). Two observations are particularly significant: Firstly, the disintegrated particles were found to consist of smaller cobalt clusters in close proximity, with approximate diameters from 8 to 14 nm, as observed previously during the reduction step. This indicates that the dissociated particles may result from species which have not completely aggregated together into a larger particle during synthesis or initial activation. The same "cluster-like" composition was not observed for the intact particles, which were rather present as single entities, leading to two clearly distinct cobalt particle compositions. In combination with a probable different sample environment for those particles within the zeolite structure compared to those exposed to the outer lamella surface, this may explain the differing behavior of the various cobalt particles. The second observation is the presence of ordered layers of a previously unobserved material around the surface of some of the cobalt particles (Figure S19 and S21, SI). The low contrast and small atomic distances in the range of about 0.34 nm indicate that this may be graphitic carbon,[62] potentially formed through interaction of the H_2/CO reaction mixture with the cobalt catalyst.[63] While the graphitic species were observed for the disintegrated particles and stabilization from carbon deposition cannot be excluded, for the intact particles no carbon species were detected and therefore stabilization is possibly an effect of the chemical environment.

Observations on sinter stability of encapsulated Co/HZSM-5

In light of the findings from the ETEM study, which clearly indicate complex transformations in cobalt particle size under reaction conditions, the changes in methane and carbon dioxide selectivity at constant temperature of 250 °C are discussed in consideration of the aforementioned pressure gap between *in situ* and *ex situ* studies. On the one hand, smaller cobalt particle sizes facilitate methane selectivity[64] and are prone to be oxidized by water vapor, which additionally promotes methane selectivity.[65] These species were detected in the ETEM study as the disintegrated particles maintaining the dispersed state after 66 min at 700 °C in syngas. In contrast, particle sintering by Ostwald ripening, as found during *in situ* experiments for particles close to or breaching the surface of the lamella, favors the water adsorption at the cobalt surface, which leads to an increase in CO_2 selectivity. The same effect is known for high water partial pressure, as well.[66] Finally, a decrease in methane selectivity might be induced by blocking of cobalt sites with graphitic carbon,[67] which is in agreement with carbon deposit formation detected for *in situ* HRTEM images. Thus, the decreasing methane and increasing carbon dioxide selectivity observed during CO hydrogenation conditions indicates changes in cobalt particle size, consistently detected via ETEM. Even though the obtained data does not allow any quantitative analysis so far, the selectivity effects are most probably caused by size changes of the cobalt particles located at the external surface of the zeolite crystals, since possibly encapsulated particles are rather stable under reaction conditions.

The proposed deactivation pathways depending on the location of the cobalt particles within the zeolite matrix are shown in Figure 6. For the cobalt particles located on the external surface of the zeolite crystal (blue) sintering, re-oxidation and coking are possible deactivation mechanisms in agreement with the discussed observations. For the embedded cobalt particles (red), however, sintering can be excluded as supported by the TEM results after CO hydrogenation, due to the size restriction and rigid structure of the zeolite crystal. Thus, re-oxidation and coking are likely to contribute to catalyst deactivation for encapsulated particles even though no obvious carbon deposition was detected after the CO hydrogenation experiment. Furthermore, we conclude that the zeolite crystals remain intact during reaction, as neither cracks nor cracking into smaller particles was observed for the spent materials.

Conclusions

The bottom-up synthesis of a cobalt based zeolite material lead to a catalyst consisting of cobalt nanoparticles in different locations within a zeolitic matrix, offering micropores with a size of 9.3 Å and a good catalytic activity for CO hydrogenation. These materials were found to be a well-suited model system to investigate structural transformations by microscopic techniques. The *ex situ* and *in situ* TEM results on the Co/HZSM-5

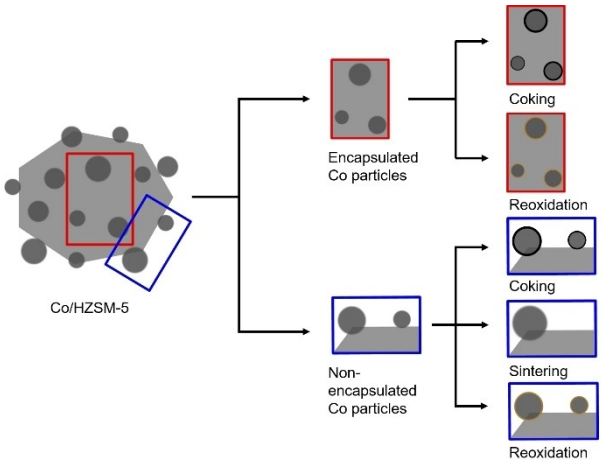

Figure 6. Possible transformations and deactivation mechanisms of cobalt species in material C during CO hydrogenation both embedded in the zeolite matrix (red) and located at the external surface of the zeolite crystal (blue).

catalyst indicate a high stability for the cobalt particles located deep within the zeolite crystal, which appeared to depend on the local structural environment. From *ex situ* TEM investigations of the spent catalyst sample after 1200 h TOS, differing behavior of the cobalt particles depending on the location in the zeolite crystal was detected. Cobalt nanoparticles encapsulated in the zeolite matrix showed almost no change in particle size, while those located at the external surface of the zeolite crystal exhibited an increase in particle size along with broadening of the particle size distribution. *In situ* TEM measurements under model conditions indicated two different behaviors of the cobalt species depending on the chemical surroundings. These two species are likely to be (i) particle clusters which remain deep within the zeolite matrix, and (ii) those which are exposed to the surface due to FIB preparation or by the synthesis procedure. While the former represents the expected structural form in the native particle-shell catalyst, the latter can be regarded as species not stabilized by steric constraints of the zeolite lattice, which is typical for standard catalysts prepared by deposition of the active phase onto the internal surface of porous substrates. The reduction from Co_3O_4 to cobalt metal leads to a shrinkage in particle size of about 30%. This observation is, though, only valid for the intact particles, the others were already disintegrated at the reduction step. For the intact particles no sintering could be observed in ETEM studies under model reaction conditions up to 1000 °C, which points towards stable cobalt particles under the harsh conditions applied. This conclusion is confirmed with CO hydrogenation reaction under reaction conditions typical for FT synthesis with a stable catalytic performance for 1200 h time on stream at reaction temperatures between 200 and 250 °C. In order to substantiate these conclusions, in future electron tomography studies should be conducted to further investigate the location of cobalt nanoparticles in the zeolite crystal and the connectivity of the zeolitic pore system. This would allow elucidating possible migration pathways and growth mechanisms of the cobalt nanoparticles. Additionally, further *in situ* analytical TEM studies would be necessary to explore the stability of the cobalt nanoparticles under reaction conditions depending on their location within the zeolite crystal.

Acknowledgements

The authors would like to thank Gregor Neusser from FIB Center of Ulm University for the sample preparation of the lamellas onto the Wildfire chips. Philipp Schlender from Institute of Inorganic Chemistry II at TU Dresden and László Eifert from Helmholtz Institute Ulm are kindly thanked for the powder X-ray diffraction measurements. Angela Straß-Eifert is grateful to Gabrielle Wiest-Danner from Institute of Chemical Engineering at Ulm University for TEM and SEM images of the samples. Thomas Diemant from Institute of Surface Chemistry and Catalysis at Ulm University is acknowledged for the X-ray photoelectron spectroscopy measurement. Furthermore, we thank Nadine Kruse from Institute of Chemical and Electrochemical Process Engineering at TU Clausthal for performing the Fischer-Tropsch experiment. Jakob Birkedal Wagner of DTU Nanolab is kindly acknowledged for helpful discussions on the manuscript and results. This work was supported by the Bundesministerium für Bildung und Forschung (BMBF) project "MicTomoCat" (05K16VK1) and partially by the Deutsche Forschungsgemeinschaft (DFG) through grant GU 1294/2. This work was supported by a research grant (9455) from VILLUM FONDEN. Open access funding enabled and organized by Projekt DEAL.

Conflict of Interest

The authors declare no conflict of interest.

Keywords: Cobalt · electron microscopy · hydrogenation · stability study · zeolite

[1] J. Bao, J. He, Y. Zhang, Y. Yoneyama, N. Tsubaki, *Angew. Chem. Int. Ed.* **2008**, *120*, 359–362.
[2] G. Prieto, H. Tüysüz, N. Duyckaerts, J. Knossalla, G.-H. Wang, F. Schüth, *Chem. Rev.* **2016**, *116*, 14056–14119.
[3] Q. Sun, X.-Q. Zhang, Y. Wang, A.-H. Lu, *Chin. J. Catal.* **2015**, *36*, 683–691.
[4] R. Güttel, T. Turek, *Energy Technol.* **2016**, *4*, 44–54.
[5] R. Xie, D. Li, B. Hou, J. Wang, L. Jia, Y. Sun, *Catal. Commun.* **2011**, *12*, 380–383.
[6] P. M. Arnal, M. Comotti, F. Schüth, *Angew. Chem. Int. Ed.* **2006**, *45*, 8224–8227; *Angew. Chem.* **2006**, *118*, 8404–8407.
[7] Q. Cheng et al., *Nat. Commun.* **2018**, *9*, 3250.
[8] Z. Zhao, *ChemCatChem* **2020**.
[9] W. Li, Y. He, H. Li, D. Shen, C. Xing, R. Yang, *Catal. Commun.* **2017**, *98*, 98–101.
[10] J. Ilsemann, A. Straß-Eifert, J. Friedland, L. Kiewidt, J. Thöming, M. Bäumer, R. Güttel, *ChemCatChem* **2019**, *11*, 4884–4893.
[11] J. D. Jimenez, C. Wen, J. Lauterbach, *Catal. Sci. Technol.* **2019**, *9*, 1970–1978.
[12] J. D. Jimenez, C. Wen, M. M. Royko, A. J. Kropf, C. Segre, J. Lauterbach, *ChemCatChem* **2019**, *12*, 846–854.
[13] S. Sartipi, M. Makkee, F. Kapteijn, J. Gascon, *Catal. Sci. Technol.* **2014**, *4*, 893–907.
[14] E. Rytter, Ø. Borg, N. E. Tsakoumis, A. Holmen, *J. Catal.* **2018**, *365*, 334–343.
[15] T. Jermwongratanachai et al., *Appl. Catal. A* **2013**, *464–465*, 165–180.
[16] Q. Zhang, J. Kang, Y. Wang, *ChemCatChem* **2010**, *2*, 1030–1058.
[17] P. R. Ellis, D. I. Enache, D. W. James, D. S. Jones, G. J. Kelly, *Nat. Can.* **2019**, *2*, 623–631.
[18] N. Kruse, A. G. Machoke, W. Schwieger, R. Güttel, *ChemCatChem* **2015**, *7*, 1018–1022.
[19] Y. Li, T. Wang, C. Wu, Y. Lv, N. Tsubaki, *Energy Fuels* **2008**, *22*, 1897–1901.
[20] X. Sun, S. Sartipi, F. Kapteijn, J. Gascon, *New J. Chem.* **2016**, *40*, 4167–4177.
[21] N. E. Tsakoumis, M. Rønning, Ø. Borg, E. Rytter, A. Holmen, *Catal. Today* **2010**, *154*, 162–182.
[22] N. E. Tsakoumis, J. C. Walmsley, M. Rønning, W. van Beek, E. Rytter, A. Holmen, *J. Am. Chem. Soc.* **2017**, *139*, 3706–3715.
[23] C. E. Kliewer, S. L. Soled, G. Kiss, *Catal. Today* **2019**, *323*, 233–256.
[24] W. Chen, I. A. W. Filot, R. Pestman, E. J. M. Hensen, *ACS Catal.* **2017**, *7*, 8061–8071.
[25] M. Claeys, M. E. Dry, E. van Steen, P. J. van Berge, S. Booyens, R. Crous, P. van Helden, J. Labuschagne, D. J. Moodley, A. M. Saib, *ACS Catal.* **2015**, *5*, 841–852.
[26] M. Rahmati, M.-S. Safdari, T. H. Fletcher, M. D. Argyle, C. H. Bartholomew, *Chem. Rev.* **2020**, *120*, 4455–4533.
[27] F. F. Tao, P. A. Crozier, *Chem. Rev.* **2016**, *116*, 3487–3539.
[28] S. Baier et al., *Microsc. Microanal.* **2017**, *23*, 501–512.
[29] J.-D. Grunwaldt, J. B. Wagner, R. E. Dunin-Borkowski, *ChemCatChem* **2013**, *5*, 62–80.

[30] M. Loewert, M.-A. Serrer, T. Carambia, M. Stehle, A. Zimina, K. F. Kalz, H. Lichtenberg, E. Saraçi, P. Pfeifer, J.-D. Grunwaldt, *React. Chem. Eng.* **2020**, *11*, 5018.
[31] K. H. Cats, J. C. Andrews, O. Stéphan, K. March, C. Karunakaran, F. Meirer, F. M. F. de Groot, B. M. Weckhuysen, *Catal. Sci. Technol.* **2016**, *6*, 4438–4449.
[32] E. D. Boyes, P. L. Gai, *Ultramicroscopy* **1997**, *67*, 219–232.
[33] B. He, Y. Zhang, X. Liu, L. Chen, *ChemCatChem* **2020**, *12*, 1853–1872.
[34] A. K. Erdamar, S. Malladi, F. D. Tichelaar, H. W. Zandbergen in *Controlled Atmosphere Transmission Electron Microscopy: Principles and Practice* (Eds.: T. W. Hansen, J. B. Wagner), Springer International Publishing, Cham, **2016**.
[35] M. Duan, J. Yu, J. Meng, B. Zhu, Y. Wang, Y. Gao, *Angew. Chem. Int. Ed.* **2018**, *57*, 6464–6469; *Angew. Chem.* **2018**, *130*, 6574–6579.
[36] P. L. Gai, E. D. Boyes, S. Helveg, P. L. Hansen, S. Giorgio, C. R. Henry, *MRS Bull.* **2007**, *32*, 1044–1050.
[37] R. W. Mitchell et al., *ACS Catal.* **2018**, *8*, 8816–8829.
[38] P. Li, J. Liu, N. Nag, P. A. Crozier, *Appl. Catal. A* **2006**, *307*, 212–221.
[39] M. R. Ward, E. D. Boyes, P. L. Gai, *ChemCatChem* **2013**, *5*, 2655–2661.
[40] R. Dehghan, T. W. Hansen, J. B. Wagner, A. Holmen, E. Rytter, Ø. Borg, J. C. Walmsley, *Catal. Lett.* **2011**, *141*, 754–761.
[41] K. Dembélé, M. Bahri, G. Melinte, C. Hirlimann, A. Berliet, S. Maury, A.-S. Gay, O. Ersen, *ChemCatChem* **2018**, *10*, 4004–4009.
[42] H. Schulz, Z. Nie, F. Ousmanov, *Catal. Today* **2002**, *71*, 351–360.
[43] J. Knochen, R. Güttel, C. Knobloch, T. Turek, *Chem. Eng. Process.* **2010**, *49*, 958–964.
[44] J. Schindelin et al., *Nat. Methods* **2012**, *9*, 676–682.
[45] J. H. Sinfelt, *Adv. Catal.* **1973**, *23*, 91–119.
[46] X. Peng, K. Cheng, J. Kang, B. Gu, X. Yu, Q. Zhang, Y. Wang, *Angew. Chem. Int. Ed.* **2015**, *54*, 4553–4556; *Angew. Chem.* **2015**, *127*, 4636–4639.
[47] Davis, Burtron H., Occelli, Mario L., Fischer-Tropsch Synthesis, Catalysts, and Catalysis. Advances and Application, CRC Press, **2009**.
[48] H. Becker, R. Güttel, T. Turek, *Chem. Ing. Tech.* **2014**, *86*, 544–549.
[49] A. Y. Khodakov, A. Griboval-Constant, R. Bechara, V. L. Zholobenko, *J. Catal.* **2002**, *206*, 230–241.
[50] S.-H. Kang, J.-H. Ryu, J.-H. Kim, P. S. Sai Prasad, J. W. Bae, J.-Y. Cheon, K.-W. Jun, *Catal. Lett.* **2011**, *141*, 1464–1471.
[51] S. Sartipi, J. E. Van Dijk, J. Gascon, F. Kapteijn, *Appl. Catal. A* **2013**, *456*, 11–22.
[52] M. Wolf, H. Kotzé, N. Fischer, M. Claeys, *Faraday Discuss.* **2017**, *197*, 243–268.
[53] J. Zhang et al., *Nat. Can.* **2018**, *1*, 540–546.
[54] J. Liu, D. Wang, J.-F. Chen, Y. Zhang, *Int. J. Hydrogen Energy* **2016**, *41*, 21965–21978.
[55] J. P. den Breejen, P. B. Radstake, G. L. Bezemer, J. H. Bitter, V. Frøseth, A. Holmen, K. P. de Jong, *J. Am. Chem. Soc.* **2009**, *131*, 7197–7203.
[56] A. Carvalho, M. Marinova, N. Batalha, N. R. Marcilio, A. Y. Khodakov, V. V. Ordomsky, *Catal. Sci. Technol.* **2017**, *7*, 5019–5027.
[57] L. Nie, Z. Li, T. Kuang, S. Lyu, S. Liu, Y. Zhang, B. Peng, J. Li, L. Wang, *Chem. Commun.* **2019**, *55*, 10559–10562.
[58] P. C. Thüne, C. J. Weststrate, P. Moodley, A. M. Saib, J. van de Loosdrecht, J. T. Miller, J. W. Niemantsverdriet, *Catal. Sci. Technol.* **2011**, *1*, 689.
[59] A. Y. Khodakov, J. Lynch, D. Bazin, B. Rebours, N. Zanier, B. Moisson, P. Chaumette, *J. Catal.* **1997**, *168*, 16–25.
[60] S. Sun, K. Fujimoto, Y. Yoneyama, N. Tsubaki, *Fuel* **2002**, *81*, 1583–1591.
[61] D. Kistamurthy, A. M. Saib, D. J. Moodley, J. W. Niemantsverdriet, C. J. Weststrate, *J. Catal.* **2015**, *328*, 123–129.
[62] P. L. d. Andres, R. Ramirez, J. A. Verges, *Phys. Rev. B* **2008**, *77*, 97.
[63] G. M. Bremmer, E. Zacharaki, A. O. Sjåstad, V. Navarro, J. W. M. Frenken, P. J. Kooyman, *Faraday Discuss.* **2017**, *197*, 337–351.
[64] D. Vervloet, F. Kapteijn, J. Nijenhuis, J. R. Van Ommen, *Catal. Sci. Technol.* **2012**, *2*, 1221.
[65] Z.-j. Wang, S. Skiles, F. Yang, Z. Yan, D. W. Goodman, *Catal. Today* **2012**, *181*, 75–81.
[66] A. Tavasoli, K. Sadaghiani, A. Nakhaeipour, M. Ahangari, *Iran. J. Chem. Chem. Eng.* **2007**, *26*, 9–16.
[67] W. Chen, R. Pestman, B. Zijlstra, I. A. W. Filot, E. J. M. Hensen, *ACS Catal.* **2017**, *7*, 8050–8060.

Manuscript received: September 21, 2020
Revised manuscript received: October 29, 2020
Accepted manuscript online: October 31, 2020
Version of record online: November 25, 2020